



**HAL**  
open science

## Bonding of xenon to oxygen in magmas at depth

Clémence Leroy, Chrystèle Sanloup, Hélène Bureau, Burkhard C. Schmidt,  
Zuzana Konôpková, Caroline Raepsaet

► **To cite this version:**

Clémence Leroy, Chrystèle Sanloup, Hélène Bureau, Burkhard C. Schmidt, Zuzana Konôpková, et al..  
Bonding of xenon to oxygen in magmas at depth. *Earth and Planetary Science Letters*, 2017, 484,  
pp.103 - 110. 10.1016/j.epsl.2017.12.019 . cea-01672802

**HAL Id: cea-01672802**

**<https://cea.hal.science/cea-01672802>**

Submitted on 16 Jan 2018

**HAL** is a multi-disciplinary open access archive for the deposit and dissemination of scientific research documents, whether they are published or not. The documents may come from teaching and research institutions in France or abroad, or from public or private research centers.

L'archive ouverte pluridisciplinaire **HAL**, est destinée au dépôt et à la diffusion de documents scientifiques de niveau recherche, publiés ou non, émanant des établissements d'enseignement et de recherche français ou étrangers, des laboratoires publics ou privés.

# Bonding of xenon to oxygen in magmas at depth

Clémence Leroy<sup>1</sup>, Chrystèle Sanloup<sup>2\*</sup>, Hélène Bureau<sup>1</sup>,  
Burkhard C. Schmidt<sup>3</sup>, Zuzana Konôpková<sup>4</sup>, Caroline Raepsaet<sup>5</sup>

<sup>1</sup>*Sorbonne Universités, UPMC Univ Paris 06, CNRS,  
Institut de Minéralogie, de Physique des matériaux et de Cosmochimie, 75005 Paris, France*

<sup>2</sup>*Sorbonne Universités, UPMC Univ Paris 06, CNRS,  
Institut des Sciences de la Terre de Paris, 75005 Paris, France*

<sup>3</sup>*Goettingen University, Geowissenschaftliches Zentrum, 37077 Goettingen, Germany*

<sup>4</sup>*DESY Photon Science, Notkestr. 85, 22607 Hamburg, Germany*

<sup>5</sup>*NIMBE, CEA, CNRS, Université Paris-Saclay, CEA Saclay, 91191 Gif-sur-Yvette, France*

\* *Corresponding author (chrystele.sanloup@upmc.fr)*

---

## Abstract

The field of noble gases chemistry has witnessed amazing advances in the last decade with over 100 compounds reported including Xe oxides and Xe-Fe alloys stable at the pressure-temperature conditions of planetary interiors. The chemistry of Xe with planetary materials is nonetheless still mostly ignored, while Xe isotopes are used to trace a variety of key planetary processes from atmosphere formation to underground nuclear tests. It is indeed difficult to incorporate the possibility of Xe reactivity at depth in isotopic geochemical models without a precise knowledge of its chemical environment. The structure of Xe doped hydrous silica-rich melts is investigated by *in situ* high energy synchrotron X-ray diffraction using resistive heating diamond anvil cells. Obtained pair distribution functions reveal the oxidation of Xe between 0.2 GPa and 4 GPa at high T up to 1000 K. In addition to the usual interatomic distances, a contribution at  $2.05 \pm 0.05$  Å is observed. This contribution is not observed in the undoped melt, and is interpreted as the Xe-O bond, with a coordination number of about 12 consistent

with Xe insertion in rings of the melt structure. Xe solubility measurements by electron microprobe and particle induced X-rays emission analysis confirm that Xe and Ar have similar solubility values in wt% in silicate melts. These values are nonetheless an order of magnitude higher than those theoretically calculated for Xe. The formation of Xe-O bonds explains the enhanced solubility of Xe in deep continental crust magmas, revealing a mechanism that could store Xe and fractionate its isotopes. Xenon is indeed atypical among noble gases, the atmosphere being notably depleted in elemental Xe, and very strongly depleted in Xe light isotopes. These observations are known as the ‘missing’ Xe paradox, and could be solved by the present findings.

---

## 1. Introduction

2 Noble gases are key tracers of Earth dynamics, and as such, Xe isotopes are impor-  
3 tant markers of planetary and atmosphere formation (Staudacher and Allègre, 1982;  
4 Pepin, 2006); they may also be used to track underground nuclear tests (Hourdin and  
5 Issartel, 2000). In particular, the I-Pu-Xe system is used to date the formation of  
6 the atmosphere (Ozima and Podosek, 1999; Avice and Marty, 2014) due to the very  
7 short half-lives of  $^{129}\text{I}$  (17 My) and  $^{244}\text{Pu}$  (82 My). Degassing of the early Earth could  
8 thus have massively contributed to the formation of the terrestrial atmosphere within  
9 the first 100 Myr (Staudacher and Allègre, 1982). However, recent Monte Carlo sim-  
10 ulations pointed out that given the uncertainties on Xe isotopic compositions, such a  
11 catastrophic early degassing event could not be evidenced unambiguously, and that the  
12 potential chemistry of Xe at depth must be solved first (Boehnke et al., 2015).

13 Xe abundances and isotopic ratios have been measured in a large variety of samples  
14 (atmosphere, fluids, rocks) and from different geological contexts, from Archean rocks  
15 (Pujol et al., 2011) to Martian meteorites (Gilmour et al., 1998). From these measure-  
16 ments, it was pointed out as early as 1970 that Xe is missing from the atmosphere of  
17 the Earth and Mars (Anders and Owen, 1977), a depletion relative to chondritic pat-  
18 terns of up to 90% (Ozima and Podosek, 1999) and known as the ‘missing Xe’ problem.  
19 Atmospheric Xe is besides strongly depleted in light isotopes (Krummenacher et al.,  
20 1962), a depletion that could be even larger if the primordial Earth composition – from  
21 which the present-day atmosphere is derived by mass-fractionation processes – is the  
22 U-Xe component instead of a solar wind or Q-planetary component (Marty et al., 2017).  
23 First high precision measurements of non-radiogenic Xe isotopes (Caffee et al., 1999)  
24 and their correlation with  $^{129}\text{Xe}/^{130}\text{Xe}$  ratio showed that the atmosphere was degassed  
25 very early after minor iodine decay in the mantle, and then underwent mass fractiona-  
26 tion. Three types of scenarios have been proposed to solve the missing Xe problem. (1)  
27 Xe may have escaped from the atmosphere, possibly after ionization (Avice and Marty,  
28 2014), (2) Xe may be hidden at depth in the core (Lee and Steinle-Neumann, 2006;  
29 Zhu et al., 2014), (3) Xe may have simply not been accreted on the planet (Dauphas,  
30 2003). The fact that Earth and Mars atmospheres are similarly depleted in light Xe  
31 isotopes (Swindle et al., 1986) nevertheless points out to a phenomenon that does not  
32 depend on the mass of the planet such as hydrodynamic escape or trapping in the deep  
33 reservoirs unique to the Earth, i.e. lower mantle and core. Besides, core formation  
34 (Kleine et al., 2002) was likely completed by the time Xe was lost around 110 My

35 (Ozima and Podosek, 1999). Discovery of Archean rocks with Xe isotopic composition  
36 falling between primitive chondrites and present Earth atmosphere (Pujol et al., 2011)  
37 indicates a storage and fractionation of Xe throughout the Archean that could even  
38 continue nowadays through subduction process. Geochemical tracing of Xe recycling in  
39 the mantle (Trieloff and Kunz, 2005; Holland and Ballentine, 2006) points indeed to an  
40 obvious link between Xe and water intake and release in subduction zones, resulting in  
41 the storage of volatiles in the subcontinental lithosphere (Broadley et al., 2016). While  
42 natural Xe concentrations are  $\sim 0.1$  ppt in granites (Allègre et al., 1986) and  $\sim 0.05$  ppt  
43 in basalts (Ozima et al., 2002), they reach 0.2 ppb in deep sea siliceous fossils (Matsuda  
44 and Matsubara, 1989) that may later enter subduction zones.

45 To understand Xe atypical behaviour, the mainstream approach has been to study  
46 the relative stability of noble gases in melts relative to the major silicate minerals by  
47 measuring partition coefficients. The results (Heber et al., 2007) span 4 orders of magni-  
48 tude for Ar, and 7 for Xe, mostly due to different interpretations of where the noble gas  
49 was incorporated, i.e. exclusively in bubble-free crystal zones or including sub-surface  
50 and small bubbles as reflecting gas release upon quenching from high  $P$ - $T$  conditions.  
51 This highlights the extreme difficulty to probe the behaviour of volatile elements by an-  
52 alyzing samples recovered at ambient conditions, either natural or synthetic. Besides,  
53 despite its generally inert nature, Xe has been shown to react with crystalline planetary  
54 oxides (Sanloup et al., 2005, 2011, 2013; Seoung et al., 2014; Crépisson et al., 2018) un-  
55 der the high pressure ( $P$ )-temperature ( $T$ ) conditions relevant of planetary interiors. Xe  
56 oxides have been synthesized at ambient  $P$  and cryogenic  $T$ :  $\text{XeO}_3$ ,  $\text{XeO}_4$ , Xe peroxides

57 ( $\text{XeO}_6^{4-}$  ion),  $\text{XeO}_2$  (Brock and Schrobilgen, 2011), and lately Xe perovskites (Britvin  
58 et al., 2016). On the high  $P$  side, Xe oxides have been predicted to be stable above  
59 75 GPa (Zhu et al., 2013; Hermann and Schwerdtfeger, 2014), and observed above 77  
60 GPa (Dewaele et al., 2016). Magmas being the most efficient transfer agents, the next  
61 natural step was to determine Xe reactivity in silicate melts at depth.

62 The first and major objective here is to solve the retention mechanisms of Xe in  
63 deep silicate melts by means of *in situ* high  $P$ - $T$  X-ray diffraction experiments. While  
64 X-ray absorption spectroscopy (XAS) is a classical method to probe the local envi-  
65 ronment of elements in crystals, and used to evidence the Xe-O bond in high  $P$  Xe  
66 oxides (Dewaele et al., 2016), it is difficult to use it for materials without appropriate  
67 standards and with unknown structure, especially disordered materials such as mag-  
68 mas. Instead, X-ray diffraction data are not model dependent. They are however  
69 not chemically-selective and all ion-ion contributions must be solved. This implies to  
70 work with simplified chemical compositions, such as haplogranitic magmas taken here  
71 as analogues of continental crust melts, with only 5 elements (Si, Al, Na, K, and O),  
72 and Si making 70 at% of the cations. X-ray diffraction is a well established technique  
73 to probe the structural environment of major cations in silicate melts *in situ*, and the  
74 recent study of Lu environment in compressed melts has demonstrated its potential to  
75 probe the local environment of minor elements (de Grouchy et al., 2017). The second  
76 objective is to measure the solubility of Xe in silica-rich melts at high  $P$ , current data  
77 under high  $P$  conditions being limited to the tholeiitic composition (Schmidt and Kep-  
78 pler, 2002), and discuss the structural data in the light of Xe solubility measurements

79 and theoretical estimates.

## 80 **2. Experimental Methods**

### 81 *2.1. Glass Synthesis*

82 The haplogranite (HPG) glass composition was chosen as a continental crust melt  
83 analogue. The starting HPG glass was prepared by mixing reagent grade oxides ( $\text{Al}_2\text{O}_3$ ,  
84  $\text{SiO}_2$ ) and carbonates ( $\text{Na}_2\text{CO}_3$ ,  $\text{K}_2\text{CO}_3$ ) powders. Powder was ground and decarbon-  
85 ated by slow ramp heating from room temperature to 1473 K within 8 hours in a  
86 platinum crucible, further fused at 1873 K in an atmospheric furnace for one hour, and  
87 quenched in water. The obtained glass was crushed into a powder, and remelted twice  
88 at 1873 K to ensure homogeneity. Hydration was done by high  $P$ - $T$  synthesis at 2 GPa  
89 and 1673 K using a piston-cylinder apparatus with a half-inch talc pyrex assembly, a  
90 graphite heater, and dried MgO powder packed around the Pt capsule. Two hydration  
91 levels were targeted, 5 wt% and 7 wt%. For that purpose, the glass was encapsulated  
92 along with the approximate amount of distilled water in a platinum capsule weld shut  
93 at both ends. Xenon doping was done subsequently by gas-loading (Boettcher et al.,  
94 1989) another platinum capsule partially filled with the recovered hydrous HPG glasses,  
95 and brought to 3.5 GPa and 1873 K for one hour, followed by rapid  $T$  quenching and  
96 decompression at room  $T$ . The major part of the capsule material was used for X-ray  
97 diffraction experiments, and a few glass pieces were spared for chemical analysis. The  
98 HPG-7wt% $\text{H}_2\text{O}$  composition was slightly contaminated upon retrieving the hydrated  
99 glass from the first platinum capsule by the MgO  $P$ -medium packed around the capsule

100 (1.5 wt% MgO, cf Table 1).

101

## 102 *2.2. Recovered Sample Analysis*

103 Starting glasses and one sample (P5) were analyzed for major elements using a  
104 CAMECA SX-FIVE electron microprobe analyzer (EMPA) at Camparis (UPMC, Paris),  
105 using a defocused beam of 15  $\mu\text{m}$  diameter and the following operating conditions: 1)  
106 15 keV accelerating voltage, 6 nA beam current for Na, K, Al, Si, and 2) 15 keV and 100  
107 nA for Xe. Calibration for Xe was established by measuring the counts for the neigh-  
108 boring elements, I (CuI) and Cs (CsCl) following the procedure developed by Montana  
109 et al. (1993). Hydrogen (i.e. water) and Xe contents were analyzed with the nuclear  
110 microprobe of LEEL/LIMBE, CEA Saclay, France using ERDA (Elastic Recoil Detec-  
111 tion Analysis) and PIXE (Particle Induced X rays Emission) respectively. For ERDA  
112 (Bureau et al., 2009) we used a  $4\times 16 \mu\text{m}^2$  incident beam of  $^4\text{He}$  at 3 MeV, mapped on  
113 selected areas (up to  $200\times 200 \mu\text{m}^2$ ). For PIXE (Bureau et al., 2000, 2010), we used a  
114  $3\times 3 \mu\text{m}^2$  incident beam of protons at 2 MeV mapped on selected areas (up to  $200\times 200$   
115  $\mu\text{m}$ ), and the Xe L X-ray line at 4.1 keV. Xe contents obtained by EMPA (Table 1) and  
116 PIXE (Fig.1) compare well, except for one sample (P5) that we attribute to the sample  
117 geometry as the sample surface could not be mirror polished, being embedded in the  
118 epoxy while still in the rhenium gasket chamber. The PIXE measurements indicate  
119 that the sample Xe content did not change during the course of the X-ray diffraction  
120 experiment.

Table 1: Chemical composition in wt% obtained from EMPA except \* from PIXE and \*\* from ERDA. Analyses are based on average of 10 data points, standard deviations are shown in brackets.

Oxide	plain glass	Xe-dopped glasses		Recovered sample P5
SiO <sub>2</sub>	73.8 (0.6)	69.3 (0.7)	71.3 (0.7)	67.9 (0.9)
Al <sub>2</sub> O <sub>3</sub>	12.2 (0.3)	11.1 (0.3)	11.7 (0.2)	10.8 (0.3)
Na <sub>2</sub> O	4.7 (0.1)	3.6 (0.1)	4.6 (0.1)	3.2 (0.5)
K <sub>2</sub> O	4.2 (0.2)	3.7 (0.2)	4.1 (0.2)	3.9 (0.1)
MgO	-	1.5 (0.1)	-	1.6 (0.1)
Xe	-	3.1 (0.2)	4.6 (0.1)	1.5 (0.2)
Xe*	-	3.1 (0.4)	4.0 (0.8)	2.9 (0.4)
H <sub>2</sub> O**	5.9 (1.7)	7.2 (2.0)	5.1 (1.4)	7.2 (2.0)
Total	100.8	99.5	100.8	97.5

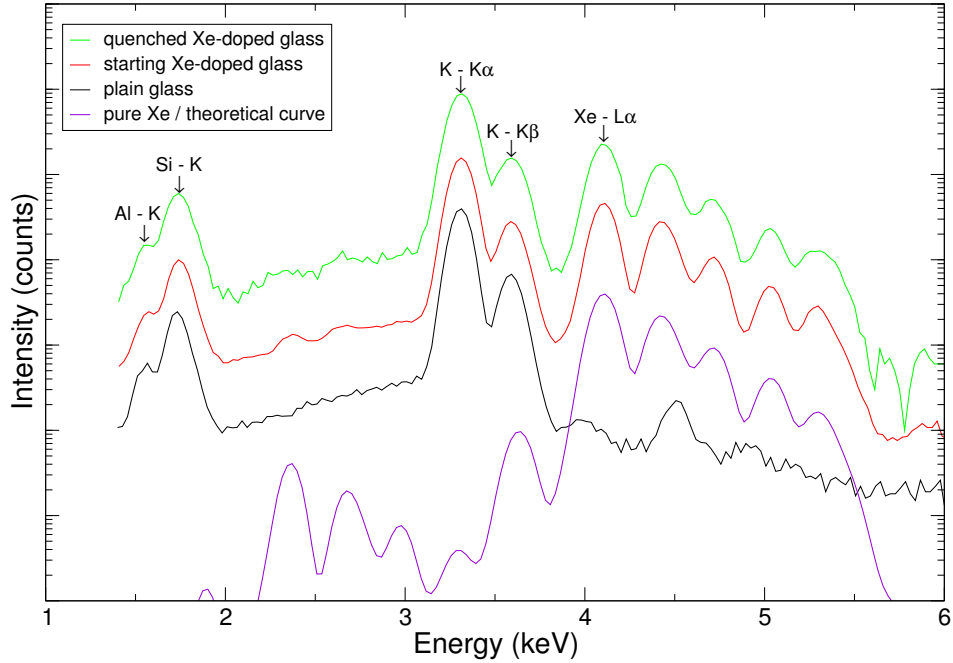


Figure 1: PIXE spectra of glasses and theoretical spectrum. Red line: starting glass (3.1 wt% Xe), green line: glass recovered from XRD run P5 (2.9 wt% Xe).

121 *2.3. X-ray Diffraction*

122 We collected *in situ* high energy synchrotron X-ray diffraction (XRD) data in re-  
 123 sistive heating diamond anvil cells at the extreme conditions beamline P02.2, Petra  
 124 III (DESY, Hamburg). High  $P$ - $T$  conditions were generated by symmetric resistive-  
 125 heating diamond-anvil cells (DAC) equipped with either 300  $\mu\text{m}$  culet diamonds and  
 126 70°-opening Boehler Almax seats (runs P5, P7, P11) or 800  $\mu\text{m}$  culet diamonds and 80°-  
 127 opening Boehler Almax seats (runs P3, P6). We used a high energy X-ray monochro-  
 128 matic beam (60 keV) focused down to 4  $\mu\text{m}$  × 6  $\mu\text{m}$  to access a wide  $q$ -range of 15  $\text{\AA}^{-1}$   
 129 (runs P5, P7, P11) to 16  $\text{\AA}^{-1}$  (runs P3, P6), allowing high spatial resolution in di-  
 130 rect space. While optimising the spatial resolution is always important in structural

131 studies, it is particularly crucial here to decipher the contribution of Xe, a minor ele-  
132 ment. Heating was achieved by an internal resistive molybdenum-wire heater, and an  
133 external heater set at 200°C around the DAC. The starting glass sample was loaded  
134 in a 200  $\mu\text{m}$  diameter hole drilled in a rhenium gasket. Pressure was measured from  
135 the fluorescence of a ruby sphere (Mao et al., 1986) at ambient  $T$ , and from the unit  
136 cell volume of platinum (Fei et al., 2004) at high  $T$ . Temperature was read by a type-  
137 K thermocouple localized as close as possible to the sample chamber. *In situ* X-ray  
138 diffraction data were collected for five different loadings (Table 2 and Fig.2), three on  
139 the HPG-3wt%Xe-7wt%H<sub>2</sub>O composition, one on the HPG-4wt%Xe-5wt%H<sub>2</sub>O com-  
140 position, and one on the undoped HPG-7wt%H<sub>2</sub>O composition. The hydrous HPG  
141 composition has a glass transition temperature low enough  $\sim 850$  K (Dingwell, 1998)  
142 to be achieved with a resistive heating furnace, and its high silica content (70 at%)  
143 implies that the melt is highly polymerized with consequent high noble gases solubility  
144 (Carroll and Stolper, 1993). The addition of water to the starting glass consequently  
145 lowered the rate of recrystallization upon heating. Recrystallization occurred above the  
146 glass transition  $T$  in only two runs, while the others remained in the amorphous state,  
147 and were quenched as glasses. At each  $P$ - $T$  point, 120 times 1 s diffraction patterns  
148 were recorded on a Perkin-Elmer 2D detector, and summed. Diffraction patterns were  
149 integrated using the Fit2D software (Hammersley et al., 1996). For each run, X-ray  
150 diffraction patterns were collected at room conditions with an empty gasket inserted in  
151 the DAC. The baseline of the recrystallized patterns (P7 and P11) was used to scale the  
152 intensity of the empty background patterns. Obtained patterns were then subtracted

153 from the sample diffraction patterns to isolate the signal scattered from the melt.

Table 2: Summary of diamond-anvil cell runs.

Run	Starting composition	Quenched products
P3	HPG-7wt%H <sub>2</sub> O	glass
P5	HPG-3wt%Xe-7wt%H <sub>2</sub> O	glass
P6	HPG-3wt%Xe-7wt%H <sub>2</sub> O	glass
P7	HPG-4wt%Xe-5wt%H <sub>2</sub> O	crystals
P11	HPG-3wt%Xe-7wt%H <sub>2</sub> O	crystals

### 154 3. Results

#### 155 3.1. Overall structural description

156 To obtain a detailed description of Xe local environment in compressed silicate  
157 melt, X-ray diffraction data were collected on both Xe-doped and plain samples as  
158 X-ray diffraction is not chemically-selective. All ion-ion contributions must be solved,  
159 which could be done in this study due to the chemical simplicity of the chosen magma  
160 composition with only 5 elements (Si, Al, Na, K, and O), and Si making 70 at% of the  
161 cations. X-ray diffraction intensity data are converted into the structure factor  $S(q)$   
162 (Fig.3A), where  $q$  is the scattering vector, using the Ashcroft-Langreth formalism. The  
163 radial distribution function  $g(r)$  (Fig.3B), that describes ion-ion contributions in real

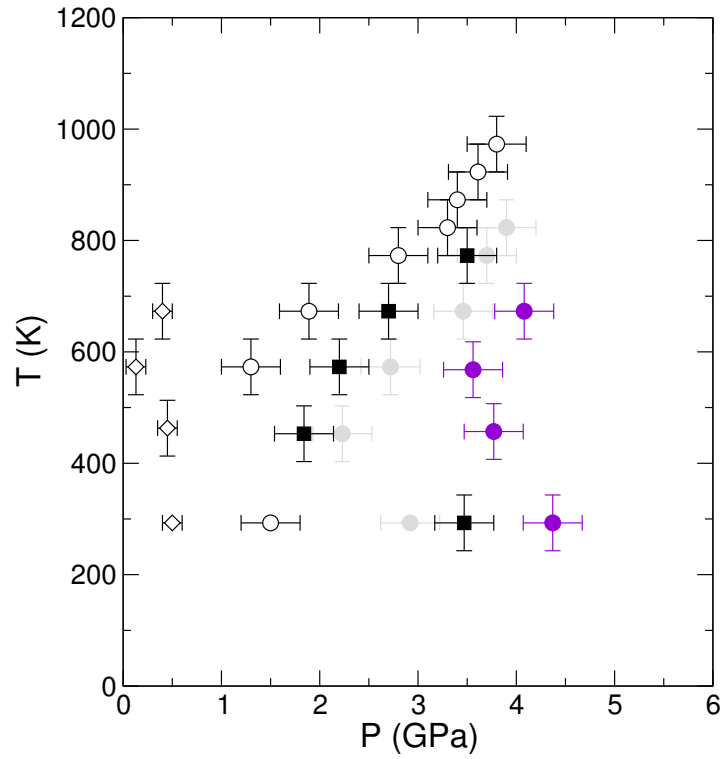


Figure 2: Experimental  $P$ - $T$  conditions. Circles: HPG-3wt%Xe-7wt%H<sub>2</sub>O composition (white: P6, purple: P11, grey: P5); diamonds: HPG-4wt%Xe-5wt%H<sub>2</sub>O composition (run P7), dark squares: plain hydrous HPG (P3).

164 space, is obtained by Fourier transforming of  $S(q)$ ,

$$g(r) = \frac{1}{2\pi^2 r n} \int_0^\infty q S(q) \sin(qr) dq \quad (1)$$

165 where  $n = \frac{\rho N_A}{M}$ ,  $M$  the mean atomic molar mass, and  $\rho$  the density calculated using  
166 the volumetric properties determined for hydrous rhyolitic liquids (Malfait et al., 2014).

167 Whereas no changes were observed for the plain composition upon heating, an addi-  
168 tional contribution is visible at  $2.05 \pm 0.05$  Å above 573 K for the Xe-doped samples,

169 and vanishes upon quenching (Fig.3B). This additional contribution is observed for all  
170 four experimental runs (Fig.1 to 3 in Supplementary Materials), and its intensity is

171 higher in run P7 for which the Xe content is higher (4 wt% *vs* 3 wt% for runs P5,  
172 P6 and P11). Amongst the atoms present in our melt composition (i.e. Si, Al, Na,

173 K, O and H), only H and O are known to form compounds with Xe (see review by  
174 Haner and Schrobilgen (2015) and references therein). Xe-H bond length in Xe-O-H

175 and Xe-C-H compounds is shorter, at 1.7-1.8 Å (Khriachtchev et al., 2008). Moreover,  
176 due to the very weak scattering factor of hydrogen, if the additional contribution at

177 2.05 Å was to be attributed to Xe-H, it would imply an extremely high coordination  
178 number. Theoretical calculations predict a much more comparable Xe-O bond length

179 of 1.99 Å to 2.29 Å in Xe-doped SiO<sub>2</sub> quartz (Probert, 2010), and of 2.17 Å in Xe-doped  
180 fibrous SiO<sub>2</sub> (Kalinowski et al., 2014), two compounds chemically close to the present

181 composition except for their crystalline state. The nature of the Xe-O bond is covalent  
182 for these predicted Xe-doped silica crystalline phases, as could also be expected from

183 the sum of the covalent radii of oxygen (0.73 Å) and xenon (1.3 Å). Despite the absence

184 of reported compounds of Xe with Si, Al, Na and K, if Xe was to interact with these  
 185 atoms in our experimental samples, one would expect an interatomic distance larger  
 186 than 2.4 Å from covalent radii considerations. For these reasons, we attribute the newly  
 187 observed peak at  $2.05 \pm 0.05$  Å to the Xe-O interatomic distance. Although no Xe-O  
 188 contribution is distinct on ambient  $T$  data, whether before or after heating, a shoulder  
 189 is still present on  $g(r)$  around 2.00 Å unlike for the plain samples (Fig.3B), indicating a  
 190 poorer ordering of Xe atoms. The second main difference between plain and Xe-doped  
 191 HPG is the stronger intensity of the first sharp diffraction peak on  $S(q)$  in the latter,  
 192 which indicates an increase of the intermediate range order.

### 193 3.2. Xenon incorporation

194 In order to estimate the Xe-O coordination number, each particular ion  $i$ -ion  $j$   
 195 partial distribution function was simulated with the following equations:

$$g_{i,j}(r) = \frac{A_{i,j}}{nS_{\infty}\sigma_i\sqrt{2\pi}} \exp\left(-\frac{(r-d_{i,j})^2}{2\sigma_{i,j}^2}\right) \quad (2)$$

196

$$A_{i,j} = \frac{CN_{i,j}}{\int \frac{4\pi r^2}{\sigma_i\sqrt{2\pi}} \exp\left(-\frac{(r-d_{i,j})^2}{2\sigma_i^2}\right) dr} \quad (3)$$

197 where  $CN_i$  is the coordination number of the ion  $i$ -ion  $j$  contribution,  $d_{i,j}$  the corre-  
 198 sponding inter-atomic distance, and  $\sigma_{i,j} = k\sqrt{d_{i,j}}$  a parameter depending on structural  
 199 disorder (Hosemann and Bagchi, 1962) where  $k$  is an adjustable parameter (typically  
 200 0.08-0.15).

$$S(q) = n \sum_{i,j} c_i c_j f_{i,j}(q) \int_0^{\infty} r(g_{i,j}(r) - 1) \frac{\sin(qr)}{k} dr \quad (4)$$

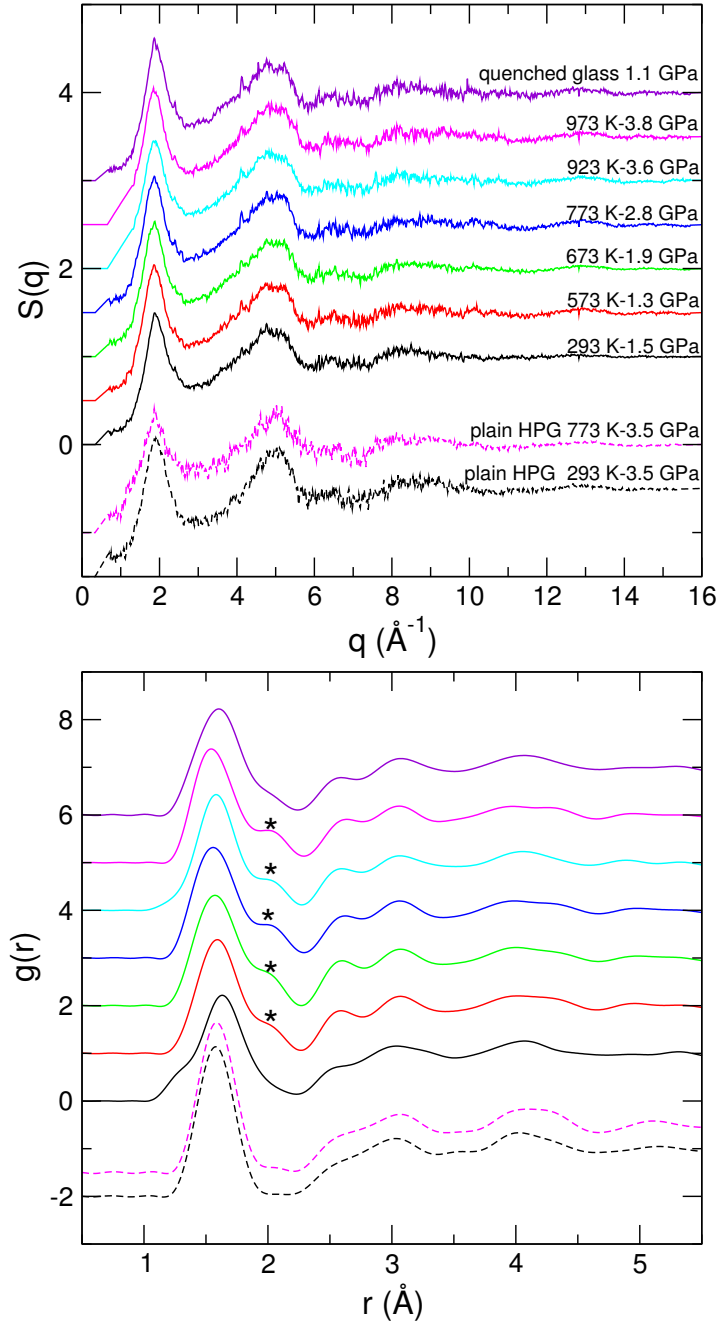


Figure 3: Structure factors,  $S(q)$ , of molten haplogranite at high pressures (top panel: runP6, see Supplementary Materials for runs P5, P7 and P11), and corresponding radial distribution functions,  $g(r)$  (bottom panel). The dotted lines correspond to the plain sample and the full lines to the Xe-doped sample. The asterisk denotes the additional contribution observed for Xe-doped samples, and attributed to the Xe-O bond.

201 with

$$f_{i,j}(q) = \frac{f_i(q)f_j(q)}{\left[\sum_i c_i f_i(q)\right]^2} \quad (5)$$

202 where  $c_i$  is the mole fraction of species  $i$ , and  $f_i$  is the atomic scattering factor tabulated  
203 from Hajdu (1972). Following the approximation adopted by Eggert et al. (2002) for  
204 polyatomic liquids, the dependency of  $f_{i,j}(q)$  on  $q$  can be removed in equation 4 and  
205 the experimental  $g(r)$  simulated directly against the weighted sum of all individual  $g_{i,j}$ .

206 Ion-ion contributions at distances larger than 2.5 Å such as K-O and Si-Si are  
207 considered negligible below the Xe-O contribution (less than 5% of the peak height), and  
208 therefore only Si-O, Al-O, and Xe-O contributions were modelled as separate gaussians,  
209 along with a single common contribution for Na-O and O-O both circa 2.5 Å, and with  
210 signal at larger distances fitted as a single large contribution (Fig.4). Both Si-O and  
211 Al-O contribute to the first peak in  $g(r)$ , while the Al content is much smaller than  
212 the Si content. Consequently, it is not possible to refine independently both Si-O and  
213 Al-O contributions. Instead, we fixed the Al-O bond length to 1.77 Å (Drewitt et al.,  
214 2015), and its coordination number to either 4.0 up to 1 GPa or 4.3 above 1 GPa. Al-O  
215 CN is indeed expected to vary between 4.0 and 4.3 in our experimental 0 GPa-3.8 GPa  
216  $P$ -range (Drewitt et al., 2015), and using either of these values provides a conservative  
217 estimate of the consequent error on the fitted Si-O coordination number of 0.05, with  
218 no significant effect on the fitted Xe-O coordination number. Fitted parameters  $CN_i$ ,  
219  $d_{i,j}$ , and  $k$  for Si-O, Al-O and Xe-O contributions at each  $P$ - $T$  condition are given in  
220 Table 3. For the plain sample (run P3), the fitted CN and bond length (respectively

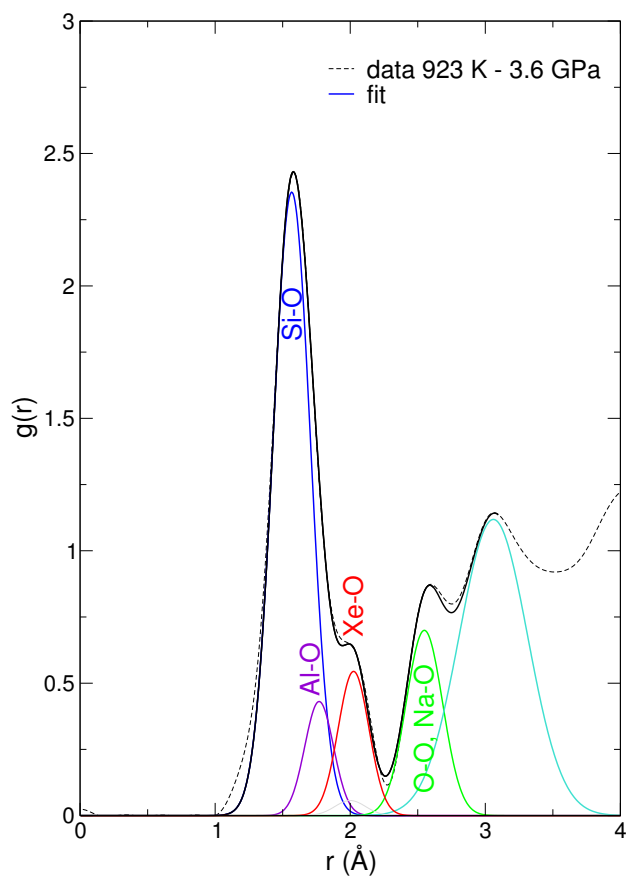


Figure 4: Fit to the experimental radial distribution function,  $g(r)$ . The black line is the sum of the underlying gaussians; only Si-O, Al-O, and Xe-O contributions were modeled as separate gaussians, along with a common contribution for Na-O and O-O both circa 2.5  $\text{\AA}$ , and with signal at larger distances fitted as a single large contribution including K-O and Si-Si at 3.1  $\text{\AA}$ ; the grey gaussian is the Mg-O contribution due to slight contamination (1.5 wt%, see section 2.1).

221 4.1 and 1.57 Å±0.02Å) for Si-O are consistent with values reported for SiO<sub>2</sub> glass at  
222 similar  $P$ , i.e. respectively 4.0 and 1.58 Å (Benmore et al., 2010). Except for the room  
223  $T$  data, the fitted Xe-O coordination number is  $12 \pm 2$ , with no dependence on either  
224  $T$  or  $P$  in the investigated  $P$ - $T$  range. Noteworthy is the systematic shift of the fit Si-O  
225 bond length upon heating to lower distances compared to the plain sample patterns  
226 (cf Table 3). This reduction of the Si-O bond length is accompanied, although less  
227 systematically, by a decrease of the Si-O coordination number. This changes in the  
228 Si-O contribution might compensate the charge transfer between Xe and O atoms.

229 The high coordination number found here is not consistent with Xe substitution  
230 to Si as proposed for quartz in the deep crust (Sanloup et al., 2005; Probert, 2010).  
231 Instead, it is consistent with the insertion of Xe in melt rings structure. Amorphous  
232 silica is characterized by a broad distribution spread between four and eight-membered  
233 rings (Huang et al., 2012), with a characteristic ring size close to 6 in compressed SiO<sub>2</sub>  
234 melts (Guerette et al., 2015). The center of these 6-membered rings is surrounded by 6  
235 oxygens in the ring plane at circa 2.2 Å (Guerette et al., 2015), with a second nearest  
236 shell of another 6 oxygens off plane. The presence of Xe could therefore stabilize the  
237 6-membered rings of the melt network, hence explaining the observed increase in in-  
238 termediate range order in the presence of Xe. The stronger intensity of the first sharp  
239 diffraction peak can indeed be interpreted as a narrowed distribution of ring sizes, with  
240 6-membered rings being more prominent compared to the broader distribution present  
241 in the plain HPG melt. Noble gases enter the melt ring structure, and as a consequence  
242 are more soluble in highly polymerized siliceous melts (Carroll and Stolper, 1993). In

Table 3: Fitting parameters derived for Si-O and Xe-O ion-ion contributions for all runs;  $CN_i$ : coordination number,  $d_i$ : bond length,  $k_i$ : width parameter of Gaussian. Error bars for Si-O and Al-O variable parameters do not vary and are given in the top row, they do vary for Xe-O as this contribution varies between ambient  $T$  and high  $T$ .

run # $P$ - $T$ conditions	Si-O			Al-O		Xe-O		
	CN	$d$ (Å)	$k$	CN	$k$	CN	$d$ (Å)	$k$
error bars	0.25	0.02	0.002	-	0.01			
<b>P3 (no Xe)</b>								
293 K-3.5 GPa	4.10	1.57	0.092	4.3	0.08	-	-	-
773 K-3.5 GPa	4.10	1.57	0.092	4.3	0.08	-	-	-
<b>P5 (3 wt% Xe)</b>								
293 K-2.9 GPa	3.93	1.58	0.150	4.3	0.14	10.8(21)	2.05(2)	0.085
453 K-2.2 GPa	3.70	1.55	0.140	4.3	0.14	12.6(4)	2.03(2)	0.080
573 K-2.7 GPa	3.70	1.56	0.120	4.3	0.14	13.0(2)	2.05(2)	0.078
773 K- 3.7 GPa	3.75	1.53	0.145	4.3	0.14	12.9(2)	2.03(2)	0.080
quench 2.5 GPa	3.87	1.57	0.120	4.3	0.14	12.0(4)	2.06(2)	0.084
<b>P6 (3 wt% Xe)</b>								
293 K-1.5 GPa	3.75	1.62	0.120	4.0	0.12	4.1(5)	2.02(2)	0.100
573 K-1.3 GPa	4.03	1.57	0.120	4.3	0.09	10.3(4)	2.02(2)	0.080
673 K-1.9 GPa	4.00	1.56	0.120	4.3	0.08	12.4(2)	2.00(2)	0.080
773 K-2.8 GPa	4.10	1.55	0.120	4.3	0.08	13.8(2)	2.03(2)	0.080
923 K-3.4 GPa	4.06	1.57	0.110	4.3	0.08	12.7(3)	2.03(2)	0.080
973 K-3.8 GPa	3.87	1.54	0.110	4.3	0.08	13.4(2)	2.02(2)	0.080
quench 1.1 GPa	3.93	1.58	0.130	4.0	0.10	6.0(5)	2.01(2)	0.085
<b>P7 (4 wt% Xe)</b>								
293 K-0.5 GPa	3.55	1.58	0.133	4.0	0.14	12.2(7)	2.05(2)	0.085
483 K-0.45 GPa	3.55	1.54	0.138	4.0	0.14	11.5(2)	2.05(2)	0.080
573 K-0.13 GPa	3.55	1.55	0.132	4.0	0.14	12.0(2)	2.05(2)	0.080
673 K-0.4 GPa	3.61	1.55	0.137	4.0	0.14	13.3(2)	2.05(2)	0.080
<b>P11 (3 wt% Xe)</b>								
293 K-4.4 GPa	3.95	1.54	0.150	4.3	0.14	9.0(10)	2.07(4)	0.120
457 K-3.8 GPa	3.73	1.53	0.140	4.3	0.14	11.9(2)	2.05(2)	0.090
588 K-3.6 GPa	3.88	1.54	0.125	4.3	0.11	10.3(3)	2.10(2)	0.090
693 K-4.1 GPa	3.82	1.53	0.125	4.3	0.11	12.7(2)	2.08(2)	0.088
773 K-4.2 GPa	3.90	1.53	0.120	4.3	0.11	11.4(2)	2.07(2)	0.080

243 the case of Kr dissolved in vitreous silica (Wulf et al., 1999), the oxygen atoms lie at  
244 a significantly greater distance of 3.45 Å compared to the Xe-O distance of  $2.05 \pm 0.05$   
245 Å found in the compressed silicate melts, consistent with Kr being a neutral species in  
246 vitreous silica. There are no experimental indications on the valence of Xe in silica-rich  
247 melts. Xe has a +5.08 valence in Xe-doped fibrous silica (Kalinowski et al., 2014), the  
248 closest crystalline analogue to our silica-rich melts in terms of chemical composition,  
249 with a coordination number of 4 and mean bond length of 2.17 Å. Amongst all reported  
250 Xe oxides, Xe valence varies from +2.89 in Xe-doped olivine for a coordination number  
251 of 3 and bond length circa 2.0 Å (Crépeisson et al., 2018), to +8 for Xe in XeO<sub>4</sub> (co-  
252 ordination number of 4, bond length of 1.74 Å (Gundersen and Hedberg, 1970)) and  
253 K<sub>4</sub>Xe<sub>3</sub>O<sub>12</sub> perovskite (coordination number of 6, bond length of 1.77 Å (Britvin et al.,  
254 2016)). From this review, no systematic trend appears between Xe-O coordination  
255 number, valence and/or bond length; however the Xe-O bond always has a covalent  
256 character, and a minimum valence of +4 for Xe in compressed silicate melts seems a  
257 conservative assumption.

### 258 *3.3. Xe solubility*

259 Our measured solubility values of Xe at 3.5 GPa in molten hydrous HPG, i.e.  
260 3.1(0.4) wt% for 7.2 wt% H<sub>2</sub>O and 4.0(0.8) wt% for 5.1 wt% H<sub>2</sub>O, are respectively  
261 5 and 7 times higher than Xe solubility in tholeitic melt (Schmidt and Keppler, 2002).  
262 The lower solubility of Xe in the most hydrated HPG glass is consistent with noble  
263 gas solubility being highest in the most polymerized melts (Carroll and Stolper, 1993),

264 water being an effective depolymerizing agent in silicate melts. Similarly, Schmidt  
265 and Keppler (2002) reported Ar solubility values about 5 times higher in molten HPG  
266 than in molten tholeite. The experimental solubility values are however at odds with  
267 molecular dynamic calculations (Guillot and Sator, 2012), being a factor of 8 higher  
268 for Xe in tholeitic melt, and 10 higher for Xe in HPG melt (Fig.5). We propose that  
269 such a strong discrepancy is related to the chemical interaction between Xe and neigh-  
270 bouring O atoms that is not considered in theoretical calculations but likely enhances  
271 Xe solubility in silicate melts. Indeed, considering a neutral Xe atom implies a larger  
272 atomic radius than an oxidized Xe atom, hence the much lower abundance of sites large  
273 enough to accommodate neutral Xe atoms that does not match experimentally mea-  
274 sured solubilities. Simulations allowing Xe to ionize would be expected to reproduce  
275 the solubility data. A structural investigation of Xe environment in basaltic melts using  
276 X-ray diffraction as done here for HPG melts is not possible, due to the low Xe solubility  
277 for this composition. The very weak Xe contribution to the pair distribution functions  
278 would indeed be below noise level. The similar mismatch between experimental and  
279 theoretical Xe solubility values in molten HPG and basalt nonetheless indicates that  
280 Xe oxidation may as well occur in basalts at depth.

#### 281 **4. Discussion**

282 Xe oxidation in deep magmas and consequent isotopic fractionation may be expected  
283 in the following geodynamical settings. Xe oxidation can occur in major crystalline  
284 phases of the deep continental crust (Sanloup et al., 2005; Probert, 2010; Kalinowski

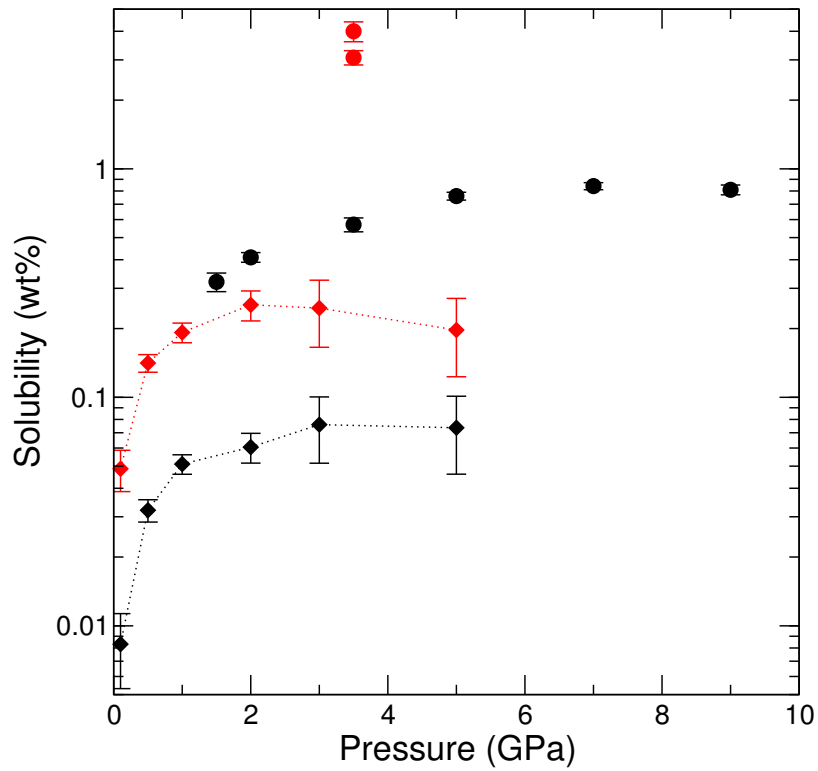


Figure 5: Experimental solubility data for Xe; black circles: in tholeiitic melt (Schmidt and Keppler, 2002), red circles: in hydrous haplogranitic melts (this work). Are shown for comparison theoretical calculations by Guillot and Sator (2012) (black diamonds: tholeiitic melt, red diamonds: haplogranitic melt).

285 et al., 2014) and upper mantle (Sanloup et al., 2011; Crépisson et al., 2018). The present  
286 experimental results show that Xe oxidation could also occur in magmas generated  
287 at subduction zones, following fluid and/or melt release from the subducted plate.  
288 Hydrous silicic slab-derived melts which composition is similar to ours occur either by  
289 melting of the basaltic crust (Prouteau et al., 2001) or by melting of siliceous sediments  
290 (Turner et al., 2012), the latter interestingly having a strong Xe retention (Matsuda and  
291 Matsubara, 1989). These melts and their metasomatic products are subsequently found  
292 in the continental lithosphere. Xe terrestrial deep cycle is therefore likely controlled by  
293 the behaviour of silica-rich materials (i.e. siliceous sediments, polymerized crustal melts  
294 and their crystallization products), providing a storage mechanism in these materials  
295 at depth. Geochemical tracing of Xe also suggests that Xe is stored in the continental  
296 lithosphere (Broadley et al., 2016), including in the deep crust where elemental and  
297 isotopic excesses have been reported (Pujol et al., 2011; Holland et al., 2013). Besides  
298 deep crustal melts, other obvious Xe reservoirs at depth would be melts trapped at depth  
299 as probed by seismological data atop the 410 km (Tauzin et al., 2010), below the 670  
300 km (Schmandt et al., 2014) and at the core-mantle boundary (Garnero and McNamara,  
301 2008). The latter might be a remnant of the magma ocean, in which noble gases were  
302 dissolved (Harper, 1996), explaining the deep mantle signature of heavy noble gases.  
303 Subsequent atmosphere ejection (T-Tauri blow-off and impact erosion) resulted in the  
304 Xe present-day atmospheric signature being derived from the Xe fraction retained at  
305 depth.

306 Xe isotopes are highly fractionated in both terrestrial and martian atmospheres, by

307 30 ‰/amu. Isotopic fractionation in experimental samples remains to be measured in  
308 order to quantitatively assess how Xe oxydation at depth may solve the Xe isotopic  
309 paradox. However, experiments involving noble gas ionization resulted in mass depen-  
310 dent isotope fractionation of Xe of the order of 5-15 ‰/amu favouring heavy isotopes  
311 at 1000 K (Kuga et al., 2015). This contradicts the intuition that elements are not  
312 isotopically fractionated at high T, as also shown by nitrogen isotopes in metal/melt  
313 partitioning experiments with  $\delta^{15}N = -3.5 \pm 1.7\text{‰}$  even in the 1900-2100 K range (Li  
314 et al., 2016). From bond stiffness considerations, the effect of Xe-O bond formation in  
315 silicates is expected to be stronger than simple ionization as it involves more charge  
316 transfer ( $0 \rightarrow 4$ , cf section 3.2) than simple ionization while occurring at similar T  
317 (circa 1000 K). Xe oxydation in crystalline silica occurs in a different environment,  
318 with Xe being bonded to four oxygen atoms in a planar geometry (Probert, 2010; Kali-  
319 nowski et al., 2014). Different bonding environment in crystals and melts may also  
320 induce isotopic fractionation, that unlike elemental fractionation, should be preserved  
321 in experimental high  $P$ - $T$  samples quenched back to ambient conditions.

## 322 5. Conclusions

323 From *in situ* high energy X-ray diffraction measurements on compressed silicate  
324 melts, it is shown that Xe bonds to oxygen in hydrous haplogranitic magmas at depth.  
325 The Xe-O bond length is  $2.05 \pm 0.05 \text{ \AA}$  and its coordination number of  $12 \pm 2$ , consistent  
326 with Xe insertion in 6-membered rings, with 6 oxygen in the ring plane and 6 oxygen  
327 off plane. The Xe-O bond is evidenced on pair distribution functions that describe

328 the melt structure, while it is absent for Xe undoped melt. This result provides an  
329 explanation for the order of magnitude difference between experimentally measured  
330 and theoretically calculated Xe solubility in melts, while the results are in much better  
331 agreement for Ar.

332 This result adds to previous studies on Xe retention in minerals at depth, comfort-  
333 ing the hypothesis of Xe storage at depth to explain the ‘missing Xe’ paradox. To what  
334 extent Xe retention in silicate minerals and melts affects its partitioning in magmatic  
335 processes depends on crystal/melt partition coefficients. Measuring Xe crystal/melt  
336 partitioning on samples quenched to ambient conditions has proved challenging, as  
337 demonstrated by the results spanning 7 orders of magnitude (Heber et al., 2007). In-  
338 stead, a comprehensive understanding of Xe environment in melts and major silicate  
339 minerals would help to provide a theoretical framework to model Xe partitioning. This  
340 method was initially proposed by Brooker et al. (2003), although the authors then  
341 assumed zero charge neutrality for Xe, and would need to be revised to consider Xe  
342 oxidation and the consequent smaller radius of Xe.

343 This study therefore paves the way for a more systematic study of Xe chemical  
344 environment in planetary materials, extended to crystalline phases. Understanding the  
345 chemical environment of noble gases in planetary materials seems the most efficient  
346 path to solve the fundamental geochemistry of xenon.

## 347 **6. Acknowledgements**

348 We acknowledge M. Fialin for assistance with the electron microprobe analyses, and  
349 H. Khodja and S. Surblé for assistance with the nuclear microprobe analyses. Portions  
350 of this research were carried out at the light source PETRA III at DESY, a member of  
351 the Helmholtz Association (HGF). This work was supported by the European Commu-  
352 nity's Seventh Framework Programme (FP7/2007-2013) under grant agreements no.  
353 312284 and 259649 (European Research Council starting grant to C.S.), and from  
354 French state funds managed by the ANR within the Investissements d'Avenir pro-  
355 gramme under reference ANR-11-IDEX-0004-02 (cluster of Excellence MATISSE led  
356 by Sorbonne Universités).

357 **7. References**

358 Allègre, C. J., Staudacher, T., Sarda, P., 1986. Rare gas systematics: formation of the  
359 atmosphere, evolution and structure of the earth's mantle. *Earth Planet. Sci. Lett.*  
360 81, 127–150.

361 Anders, E., Owen, T., 1977. Mars and Earth: Origin and abundance of volatiles. *Science*  
362 198, 453–465.

363 Avice, G., Marty, B., 2014. The iodine-plutonium-xenon age of the Moon-Earth system  
364 revisited. *Phil. Trans. R. Soc. A* 372, 20130260.

365 Benmore, C. J., Soignard, E., Amin, S. A., Guthrie, M., Shastri, S. D., Lee, P. L.,  
366 Yarger, J. L., 2010. Structural and topological changes in silica glass at pressure.  
367 *Phys. Rev. B* 81, 054105.

368 Boehnke, P., Caffee, M. W., Harrison, T. M., 2015. Xenon isotopes in the MORB  
369 source, not distinctive of early global degassing. *Geophys. Res. Lett.* 42, 4367–4374.

370 Boettcher, S. L., Guo, Q., Montana, A., 1989. A simple device for loading gases in  
371 high-pressure experiments. *Am. Mineral.* 74, 1383–1384.

372 Britvin, S. N., Kashtanov, S. A., Krivovichev, S. V., Chukanov, N. V., 2016. Xenon in  
373 Rigid Oxide Frameworks: Structure, Bonding and Explosive Properties of Layered  
374 Perovskite  $K_4Xe_3O_{12}$ . *J. Am. Chem. Soc.* 138 (42), 13838–13841.

- 375 Broadley, M. W., Ballentine, C. J., Chavrit, D., Dallai, L., Burgess, R., 2016. Sedi-  
376 mentary halogens and noble gases within Western Antarctic xenoliths: Implications  
377 of extensive volatile recycling to the sub continental lithospheric mantle. *Geochim.*  
378 *Cosmochim. Acta* 176, 139–156.
- 379 Brock, D. S., Schrobilgen, G. J., 2011. Synthesis of the missing oxide of xenon,  $\text{XeO}_2$ ,  
380 and its implications for Earth’s missing xenon. *J. Am. Chem. Soc.* 133, 6265–6269.
- 381 Brooker, R. A., Du, Z., Blundy, J. D., Kelley, S. P., Allan, N. L., Wood, B. J., Chamorro,  
382 E. M., Wartho, J.-A., Purton, J. A., 2003. The ‘zero charge’ partitioning behaviour  
383 of noble gases during mantle melting. *Nature* 423, 738–741.
- 384 Bureau, H., Foy, E., Raepsaet, C., Somogyi, A., Munsch, P., Simon, G., Kubsky, S.,  
385 2010. Bromine cycle in subduction zones through in situ Br monitoring in diamond  
386 anvil cells. *Geochim. Cosmochim. Acta* 74, 3839–3850.
- 387 Bureau, H., Keppler, H., Métrich, N., 2000. Volcanic degassing of bromine and iodine:  
388 Experimental fluid/melt partitioning data and applications to stratospheric chem-  
389 istry. *Earth Planet. Sci. Lett.* 183, 51–60.
- 390 Bureau, H., Raepsaet, C., Khodja, H., Carraro, A., Aubaud, C., Kubsky, S., 2009.  
391 Determination of hydrogen content in geological samples using elastic recoil detection  
392 analysis (ERDA). *Geochim. Cosmochim. Acta* 73, 3311–3322.
- 393 Caffee, M. W., Hudson, G. B., Velsko, C., Huss, G. R., Alexander, E. C. J., Chivas,

394 A. R., 1999. Primordial noble gases from Earth's mantle: Identification of a primitive  
395 volatile component. *Science* 285, 2115–2118.

396 Carroll, M., Stolper, E., 1993. Noble gas solubilities in silicate melts and glasses: New  
397 experimental results for argon and the relationship between solubility and ionic poros-  
398 ity. *Geochim. Cosmochim. Acta* 57, 5039–5051.

399 Crépeisson, C., Blanchard, M., Lazzeri, M., Balan, E., Sanloup, C., 2018. New con-  
400 straints on Xe incorporation mechanisms in olivine from first-principles calculations.  
401 *Geochim. Cosmochim. Acta* 222, 146–155.

402 Dauphas, N., 2003. The dual origin of the terrestrial atmosphere. *Icarus* 165, 326–333.

403 de Grouchy, C. J. L., Sanloup, C., Cochain, B., Drewitt, J. W. E., Kono, Y., Crépeisson,  
404 C., 2017. Lutetium incorporation in magmas at depth: changes in melt local envi-  
405 ronment and the influence on partitioning behaviour. *Earth Planet. Sci. Lett.* 464,  
406 155–165.

407 Dewaele, A., Worth, N., Pickard, C. J., Needs, R. J., Pascarelli, S., Mathon, O.,  
408 Mezouar, M., Irifune, T., 2016. Synthesis and stability of xenon oxides  $\text{Xe}_2\text{O}_5$  and  
409  $\text{Xe}_3\text{O}_2$  under pressure. *Nature Chemistry* 8 (8), 784–790.

410 Dingwell, D. B., 1998. The glass transition in hydrous granitic melts. *Phys. Earth*  
411 *Planet. Int.* 107, 1–8.

412 Drewitt, J. W. E., Jahn, S., Sanloup, C., de Grouchy, C., Garbarino, G., Hennet, L.,

413 2015. Development of chemical and topological structure in aluminosilicate liquids  
414 and glasses at high pressure. *J. Phys.: Cond. Matt.* 27, 105103.

415 Eggert, J. H., Weck, G., Loubeyre, P., Mezouar, M., 2002. Quantitative structure factor  
416 and density measurements of high-pressure in diamond anvil cells by x-ray diffraction:  
417 Argon and water. *Phys. Rev. B* 65, 174105.

418 Fei, Y., van Orman, J., Li, J., van Westrenen, W., Sanloup, C., Minarik, W., Hirose,  
419 K., Komabayashi, T., Walter, M., Funakoshi, K., 2004. Experimentally determined  
420 postspinel transformation boundary in  $\text{Mg}_2\text{SiO}_4$  using MgO as an internal pressure  
421 standard and its geophysical implications. *J. Geophys. Res.* 109, B02305.

422 Garnero, E. J., McNamara, A. K., 2008. Structure and dynamics of Earth's lower  
423 mantle. *Science* 320, 626–628.

424 Gilmour, J. D., Whitby, J. A., Turner, G., 1998. Xenon isotopes in irradiated alh84001:  
425 Evidence for shock-induced trapping of ancient martian atmosphere. *Geochim. Cos-*  
426 *mochim. Acta* 62, 2555–2571.

427 Guerette, M., Ackerson, M. R., Thomas, J., Yuan, F., Watson, E. B., Walker, D.,  
428 Huang, L., OCT 15 2015. Structure and Properties of Silica Glass Densified in Cold  
429 Compression and Hot Compression. *Scientific Reports* 5.

430 Guillot, B., Sator, N., 2012. Noble gases in high-pressure silicate liquids: A computer  
431 simulation study. *Geochim. Cosmochim. Acta* 80, 51–69.

- 432 Gundersen, G., Hedberg, K., 1970. Molecular structure of xenon tetroxide,  $\text{XeO}_4$ . J.  
433 Chem. Phys. 52, 812–815.
- 434 Hajdu, F., 1972. Revised parameters of the analytic fits for coherent and incoherent  
435 scattered x-ray intensities of the first 36 atoms. Acta Cryst., 250–252.
- 436 Hammersley, A. P., Svensson, S. O., Hanfland, M., Fitch, A. N., Hausermann, D.,  
437 1996. Two-dimensional detector software: From real detector to idealised image or  
438 two-theta scan. High Press. Res. 14, 235–248.
- 439 Haner, J., Schrobilgen, G. J., 2015. The chemistry of Xenon. Chem. Rev. 115, 1255–  
440 1295.
- 441 Harper, C. L., 1996. Evidence for  $^{92g}\text{Nb}$  in the early solar system and evaluation of a  
442 new *p*-process cosmochronometer from  $^{92g}\text{Nb}/^{92}\text{Mo}$ . ApJ 466, 437–456.
- 443 Heber, V. S., Brooker, R. A., Kelley, S. P., Wood, B. J., 2007. Crystal-melt partitioning  
444 of noble gases (helium, neon, argon, krypton, and xenon) for olivine and clinopyrox-  
445 ene. Geochim. Cosmochim. Acta 71, 1041–1061.
- 446 Hermann, A., Schwerdtfeger, P., 2014. Xenon suboxides stable under pressure. J. Phys.  
447 Chem. Lett. 5, 4336–4342.
- 448 Holland, G., Ballentine, C. J., 2006. Seawater subduction controls the heavy noble gas  
449 composition of the mantle. Nature 441, 186–191.
- 450 Holland, G., Lollar, B. S., Li, L., Lacrampe-Couloume, G., Slater, G. F., Ballentine,

451 C. J., 2013. Deep fracture fluids isolated in the crust since the Precambrian era.  
452 Nature 497, 357–360.

453 Hosemann, R., Bagchi, S. N., 1962. Direct Analysis of Diffraction by Matter. North-  
454 Holland, Amsterdam.

455 Hourdin, F., Issartel, J.-P., 2000. Sub-surface nuclear tests monitoring through the  
456 CTBT xenon network. Geophys. Res. Lett. 27, 2245–2248.

457 Huang, P. Y., Kurasch, S., Srivastava, A., Skakalova, V., Kotakoski, J., Krasheninnikov,  
458 A. V., Hovden, R., Mao, Q., Meyer, J. C., Smet, J., Muller, D. A., Kaiser, U., 2012.  
459 Direct imaging of a two-dimensional silica glass on graphene. Nano Letters 12 (2),  
460 1081–1086.

461 Kalinowski, J., Rasanen, M., Gerber, R. B., 2014. Chemically-bound xenon in fibrous  
462 silica. Phys. Chem. Chem. Phys. 16, 11658–11661.

463 Khriachtchev, L., Isokoski, K., Cohen, A., Räsänen, M., Gerber, R. B., 2008. A small  
464 neutral molecule with two noble-gas atoms: HXeOXeH. J. Am. Chem. Soc. 130,  
465 6114–6118.

466 Kleine, T., Münker, C., Mezger, K., Palme, H., 2002. Rapid accretion and early core  
467 formation on asteroids and the terrestrial planets from Hf-W chronometry. Nature  
468 418, 952–955.

469 Krummenacher, D., Merrihue, C. M., Pepin, R. O., Reynolds, J. H., 1962. Meteoritic

470 krypton and barium versus the general isotopic anomalies in xenon. *Geochim. Cos-*  
471 *mochim. Acta* 26, 231–249.

472 Kuga, M., B.Marty, Marrocchi, Y., Tissandier, Y., 2015. Structure and hydrogen or-  
473 dering in ices vi, vii and viii by neutron powder diffraction. *Proc. Natl. Acad. Sci.*  
474 *U.S.A.* 112, 7129–7134.

475 Lee, K. M., Steinle-Neumann, G., 2006. High-pressure alloying of iron and xenon:  
476 “Missing” Xe in the Earth’s core? *J. Geophys. Res.* 111, B02202.

477 Li, Y., Marty, B., Shcheka, S., Zimmermann, L., Keppler, H., 2016. Nitrogen isotope  
478 fractionation during terrestrial core-mantle separation. *Geochem. Persp. Let.* 2, 138–  
479 147.

480 Malfait, W. J., Seifert, R., Petitgirard, S., Perrillat, J.-P., Mezouar, M., Ota, T., Naka-  
481 mura, E., Lerch, P., Sanchez-Valle, C., 2014. Supervolcano eruptions driven by melt  
482 buoyancy in large silicic magma chambers. *Nat. Geoscience* 7, 122–125.

483 Mao, H. K., Xu, J., Bell, P. M., 1986. Calibration of the ruby pressure gauge to 800  
484 kbar under quasi-hydrostatic conditions. *J. Geophys. Res.* 91, 4673–4676.

485 Marty, B., Altwegg, K., Balsiger, H., Bar-Nun, A., Bekaert, D. V., Berthelier, J.-J.,  
486 Bieler, A., Briois, C., Calmonte, U., Combi, M., ad B. Fiethe, J. D. K., Fuselier, S.,  
487 Gasc, S., Gombosi, T. I., Hansen, K. C., Hässig, M., Jäckel, A., Kopp, E., Korth, A.,  
488 Roy, L. L., Mall, U., Mousis, O., Owen, T., Rème, H., Rubin, M., Sémon, T., Tzou,

- 489 C.-Y., Waite, J. H., Wurz, P., 2017. Xenon isotopes in 67P/Churyumov-Gerasimenko  
490 show that comets contributed to Earth's atmosphere. *Science* 356, 1069–1072.
- 491 Matsuda, J.-I., Matsubara, K., 1989. Noble gases in silica and their implication for the  
492 terrestrial 'missing' Xe. *Geophys. Res. Lett.* 16, 81–84.
- 493 Montana, A., Guo, Q., Boettcher, S., White, B. S., Brearley, M., 1993. Xe and Ar in  
494 high-pressure silicate liquids. *Am. Mineral.* 78, 1135–1142.
- 495 Ozima, M., Miura, Y., Podosek, F., 2002. Revisiting I-Xe systematics, an early solar  
496 system chronometer. *Geochim. Cosmochim. Acta* 66 (15A, 1), A576.
- 497 Ozima, M., Podosek, F. A., 1999. Formation age of Earth from  $^{129}\text{I}/^{127}\text{I}$  and  $^{244}\text{Pu}/^{238}\text{U}$   
498 systematics and the missing Xe. *J. Geophys. Res.* 104, 25493–25499.
- 499 Pepin, R. O., 2006. Atmospheres on the terrestrial planets: Clues to origin and evolu-  
500 tion. *Earth Planet. Sci. Lett.* 252, 1–14.
- 501 Probert, M. I. J., 2010. An ab initio study of xenon retention in  $\alpha$ -quartz. *J.*  
502 *Phys.:Condens. Matter* 22, 025501.
- 503 Prouteau, G., Scaillet, B., Pichavant, M., Maury, R., 2001. Evidence for mantle meta-  
504 somatism by hydrous silicic melts derived from subducted oceanic crust. *Nature*  
505 410 (6825), 197–200.
- 506 Pujol, M., Marty, B., Burgess, R., 2011. Chondritic-like xenon trapped in Archean

507 rocks: A possible signature of the ancient atmosphere. *Earth Planet. Sci. Lett.* 308,  
508 298–306.

509 Sanloup, C., Bonev, S. A., Hochlaf, M., Maynard-Casely, H. E., 2013. Reactivity of  
510 xenon with ice at planetary conditions. *Phys. Rev. Lett.* 110, 265501.

511 Sanloup, C., Schmidt, B. C., Gudfinnsson, G., Dewaele, A., Mezouar, M., 2011. Xenon  
512 and argon: a contrasting behavior in olivine at depth. *Geochim. Cosmochim. Acta*  
513 75, 6271–6284.

514 Sanloup, C., Schmidt, B. C., Perez, E. C., Jambon, A., Gregoryanz, E., Mezouar, M.,  
515 2005. Retention of xenon in quartz and Earth’s missing xenon. *Science* 310, 1174–  
516 1177.

517 Schmandt, B., Jacobsen, S. D., Becker, T. W., Liu, Z. K., Dueker, K. G., 2014. Dehy-  
518 dration melting at the top of the lower mantle. *Science* 344, 1265–1268.

519 Schmidt, B., Keppler, H., 2002. Experimental evidence for high noble gas solubilities  
520 in silicate melts under mantle pressures. *Earth Planet. Sci. Lett.* 195, 277–290.

521 Seoung, D., Lee, Y., Cynn, H., Park, C., Choi, K.-Y., Blom, D., Evans, W. J., Kao,  
522 C.-C., Vogt, T., Lee, Y., 2014. Irreversible xenon insertion into a small-pore zeolite  
523 at moderate pressures and temperatures. *Nat. Chem.* 6, 835–839.

524 Staudacher, T., Allègre, C. J., 1982. Terrestrial xenology. *Earth Planet. Sci. Lett.* 60,  
525 389–405.

- 526 Swindle, T. D., Caffee, M. W., Hohenberg, C. M., 1986. Xenon and other noble gases in  
527 shergottites. *Geochim. Cosmochim. Acta* 50, 1001–1015.
- 528 Tauzin, B., Debayle, E., Wittlinger, G., 2010. Seismic evidence for a global low-velocity  
529 layer within the Earth’s upper mantle. *Nature Geoscience* 3, 718–721.
- 530 Trieloff, M., Kunz, J., 2005. Isotope systematics of noble gases in the Earth’s mantle:  
531 possible sources of primordial isotopes and implications for mantle structure. *Phys.*  
532 *Earth. Planet. Int.* 148, 13–38.
- 533 Turner, S., Caulfield, J., Turner, M., van Keken, P., Maury, R., Sandiford, M.,  
534 Prouteau, G., JAN 2012. Recent contribution of sediments and fluids to the mantle’s  
535 volatile budget. *Nature Geoscience* 5 (1), 50–54.
- 536 Wulf, R., Calas, G., Ramos, A., Büttner, H., Roselieb, K., Rosenhauer, M., 1999.  
537 Structural environment of krypton dissolved in vitreous silica. *Amer. Min.* 84, 1461–  
538 1463.
- 539 Zhu, L., Liu, H., Pickard, C. ., Zou, G., Ma, Y., 2014. Reactions of xenon with iron  
540 and nickel are predicted in the Earth’s inner core. *Nat. Chem.* 6, 645–649.
- 541 Zhu, Q., Jung, D. Y., Oganov, A. R., Glass, C. W., Gatti, C., Lyakhov, A. O., 2013.  
542 Stability of xenon oxides at high pressures. *Nat. Chem.* 5, 61–65.